

Snowball Earth ocean chemistry driven by extensive ridge volcanism during Rodinia breakup

T. M. Gernon^{1*}, T. K. Hincks², T. Tyrrell¹, E. J. Rohling^{1,3} and M. R. Palmer¹

During Neoproterozoic Snowball Earth glaciations, the oceans gained massive amounts of alkalinity, culminating in the deposition of massive cap carbonates on deglaciation. Changes in terrestrial runoff associated with both breakup of the Rodinia supercontinent and deglaciation can explain some, but not all of the requisite changes in ocean chemistry. Submarine volcanism along shallow ridges formed during supercontinent breakup results in the formation of large volumes of glassy hyaloclastite, which readily alters to palagonite. Here we estimate fluxes of calcium, magnesium, phosphorus, silica and bicarbonate associated with these shallow-ridge processes, and argue that extensive submarine volcanism during the breakup of Rodinia made an important contribution to changes in ocean chemistry during Snowball Earth glaciations. We use Monte Carlo simulations to show that widespread hyaloclastite alteration under near-global sea-ice cover could lead to Ca²⁺ and Mg²⁺ supersaturation over the course of the glaciation that is sufficient to explain the volume of cap carbonates deposited. Furthermore, our conservative estimates of phosphorus release are sufficient to explain the observed P:Fe ratios in sedimentary iron formations from this time. This large phosphorus release may have fuelled primary productivity, which in turn would have contributed to atmospheric O₂ rises that followed Snowball Earth episodes.

Breakup of the Rodinia supercontinent contributed to profound environmental change during the Neoproterozoic Era (~1,000–540 million years ago (Ma)). It is thought that ice sheets reached the equator^{1,2} and global temperatures dropped to -50°C during two long-lived ‘snowball’ events: the Sturtian (Cryogenian) glaciation at circa 720–660 Ma and the Marinoan (Varanger) glaciation at circa 650–630 Ma. These globally distributed glaciations have been attributed to major continental reconfiguration episodes^{3,4}. Protracted rifting circa 750 (ref. 3)–725 Ma (ref. 5) (lasting 100–120 Myr) formed the Proto-Pacific Ocean (Fig. 1a). The Sturtian glaciation coincided with initial breakup in Canada at circa 720 Ma (ref. 6), and the Marinoan with a later phase of the same breakup event in Antarctica from 670 to 650 Ma (ref. 7). Another major breakup event between circa 615 Ma (ref. 8) and 550 Ma (ref. 9) formed the Iapetus Ocean (Fig. 1b), concurrent with the Gaskiers glaciation at circa 582–580 Ma.

It has been suggested that continental breakup led to sharp increases in riverine runoff and silicate weathering (including flood basalts¹⁰), causing enhanced CO₂ drawdown and descent into a ‘snowball’ state⁴; and deglaciation resulted from gradual accumulation of atmospheric CO₂ (ref. 11), probably from subaerial volcanic outgassing¹², to critical levels capable of overcoming an ice albedo effect². Intense debate centres on the source of alkalinity required to form the extensive cap carbonate sequences associated with Snowball Earth termination, and their negative $\delta^{13}\text{C}$ signatures^{2,12,13}. Carbonate sedimentation may have occurred rapidly (<10 kyr; ref. 12) owing to a post-glacial greenhouse weathering spike^{14,15} of similar duration to Quaternary deglaciation¹⁶. However, magnetopolarity reversals exhibited in some Marinoan cap carbonates suggest accumulation took place over longer timescales (≥ 100 kyr; refs 17,18). Similarly, meltback alone cannot easily explain the inferred increase in dissolved oceanic phosphate concentrations during the Tonian

and Cryogenian periods¹⁹. Despite the temporal coincidence between breakup of Rodinia and glaciations^{3,4}, no studies have yet investigated the direct impacts of volcanism associated with extensive spreading-ridge formation (Supplementary Fig. 1).

The shallow-ridge hypothesis

Here we propose the novel shallow-ridge hypothesis, which invokes ridge volcanism to drive efficient and long-lived seafloor alteration, and in conjunction with other weathering processes linked to continental breakup^{4,10,20} can reconcile many key features of Snowball Earth episodes.

Continental unzipping of the type associated with the breakup of Rodinia is accompanied by enhanced rifting and magmatism, and can coincide with an order of magnitude increase in magmatic productivity²¹. The early phase of ocean crustal development involves a period of relatively shallow marine volcanism (Fig. 1c), as the ridge axis gradually subsides²². This low-hydrostatic-pressure regime favours explosive fragmentation of lava in contact with sea water²³, yielding voluminous hyaloclastite—a pyroclastic rock dominated by juvenile angular glass fragments—along the newly formed ridge (Fig. 1d). Hyaloclastite volcanism in early rifting environments is a rapid, high-volume process, forming from volcanic centres 30–40 km wide, and producing mounds ~1.5 km high and 15–20 km wide²². Observations and empirical subsidence relationships indicate that conditions favourable for hyaloclastite formation (depths up to 2 km) would persist along the ridge for at least 20 Myr (Supplementary Fig. 2).

The quenched glass shards typical of basaltic hyaloclastites are very susceptible to alteration, largely by hydration to palagonite²⁴. This is enhanced by a high reactive surface area:volume ratio and high porosity (compared to pillow lavas) that greatly increases seawater interaction. Basaltic glass alteration involves considerable element mobilization (for example, Ca losses of ~90%; ref. 25),

¹Ocean and Earth Science, University of Southampton, European Way, Southampton SO14 3ZH, UK. ²School of Earth Sciences, University of Bristol, Bristol BS8 1RJ, UK. ³Research School of Earth Sciences, The Australian National University, Canberra, Australian Capital Territory 2601, Australia. *e-mail: Thomas.Gernon@noc.soton.ac.uk

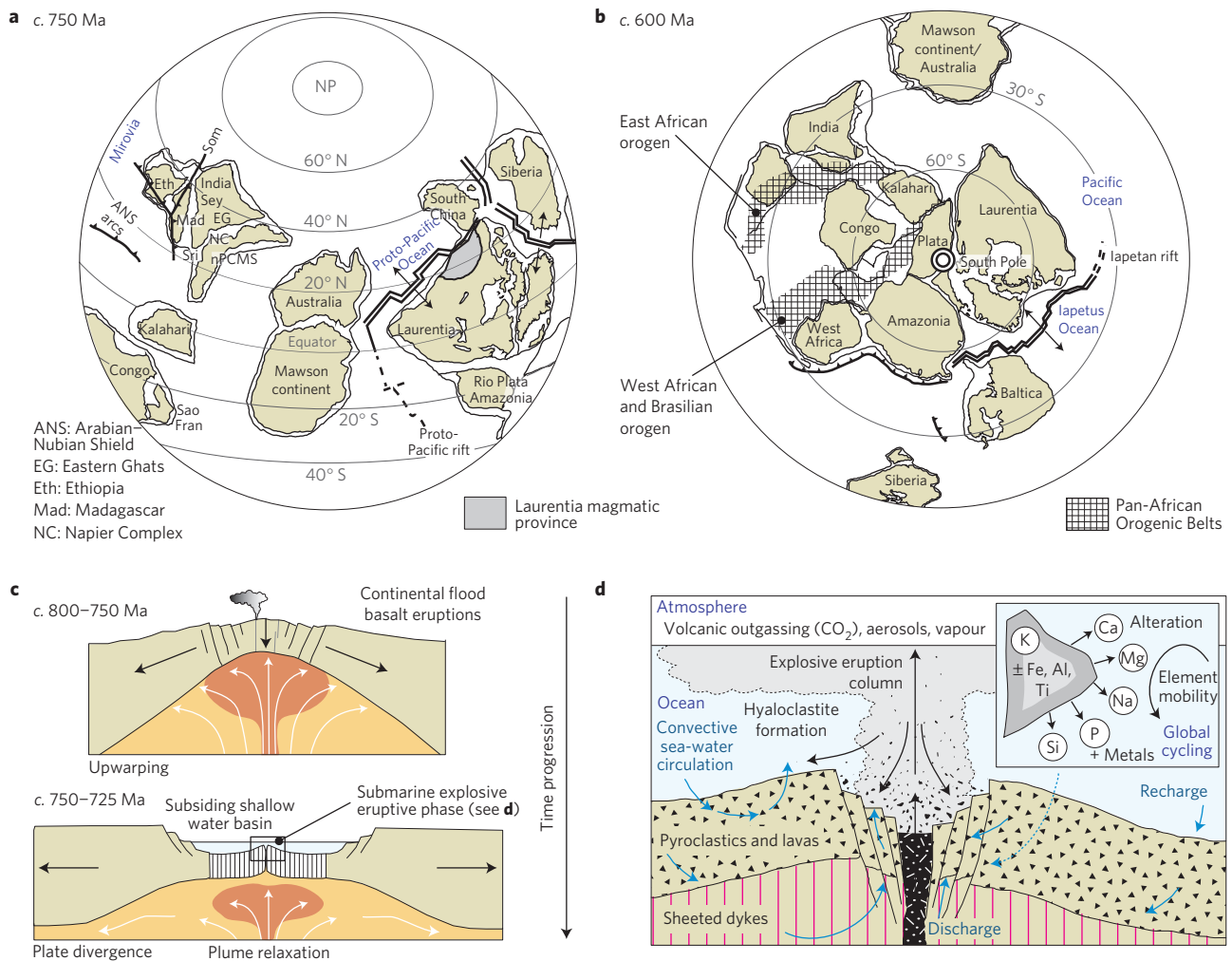


Figure 1 | Evolution of spreading-ridge systems during the late Neoproterozoic. **a, b**, Continental reconstructions at ~ 750 Ma showing the location of the Proto-Pacific rift system (**a**) and at ~ 600 Ma showing the inferred location of the Iapetus rift (**b**) (modified after ref. 10). **c**, During the early phase of plume magmatism (~ 800 Ma), volcanism was largely subaerial (Supplementary Table 1); however, as rifting occurred, the main axis of volcanism submerged below sea level, resulting in the formation of the Proto-Pacific (and Iapetus at ~ 600 Ma) and a sustained phase of shallow marine volcanism. **d**, Under these conditions (shown here before glaciation), hyaloclastites are formed preferentially by quenching and explosive shattering of lava in contact with sea water, forming 'fresh' highly alterable glasses.

and thus has the potential to exert a major control on sea-water chemistry²⁴, including consumption of aqueous CO_2 (ref. 26). The shallow ridge is also a major source of magnesium, with basaltic glass experiencing Mg losses of $\sim 67\%$ (ref. 25) to $\sim 97\%$ (ref. 24). Dissolution rates of basaltic glass could be reduced²⁴ at the low temperatures expected in an ice-covered ocean, but our model purely evaluates the initial element flux during rapid quenching, followed by cation leaching²⁴, and does not require total glass dissolution. As hyaloclastites accumulate in thick 'piles' along the ridge axis, they are susceptible to high-temperature hydrothermal circulation, leading to further losses through diffusion²⁴—conditions thought to persist for $\sim 10^6$ yr (ref. 27). Conservatively, we consider only contributions from freshly erupted material close to the ridge axis. Palagonitization of basaltic glass occurs rapidly at high temperatures²⁴, and potentially within one year in hydrothermal systems²⁸. Thus, hyaloclastite alteration can be considered almost instantaneous on geologic timescales.

This global scale process offers an alternative, complementary explanation for the surge of alkalinity associated with the Neoproterozoic "calcium ocean" and carbonate sedimentation, which cannot be satisfactorily explained by terrestrial weathering

alone²⁹. The process can also help explain the late Neoproterozoic 'excess phosphate ocean'¹⁹ and high concentrations of SiO_2 in banded iron formations (BIFs; ref. 30). Although we focus on Rodinia, shallow-ridge effects will have similarly large impacts on ocean fluxes during any major episode of continental breakup, albeit manifest in different ways owing to variations in timescales and extent of magmatic productivity, alteration and biological productivity in the ocean. It is unclear why Pangaea breakup did not result in global glaciation, although the more polar location of continents may have suppressed the continental silicate weathering CO_2 sink.

Breakup of Rodinia

The 750–725 Ma breakup involved at least $\sim 2 \times 10^4$ km spreading-ridge formation around the perimeter of Laurentia (Fig. 1a; ref. 3). Subsequent rift and drift episodes^{3,5} may have increased the total length of new spreading ridges by a factor of three to four. Although Neoproterozoic ocean crust is poorly represented in the geologic record (for example, owing to subduction), there is evidence for widespread hyaloclastite emplacement during breakup, before 'snowball' glaciations (Fig. 2). For example, the 717–716.5 Ma Mount Harper Volcanic Complex⁶—a 1.6-km-thick succession of

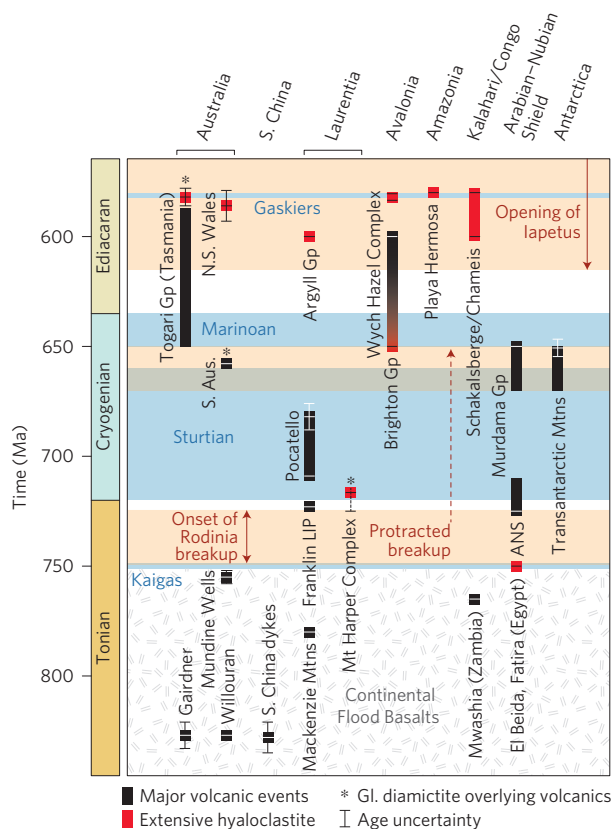


Figure 2 | Summary of major global volcanic events during the Tonian, Cryogenian and early Ediacaran periods, in relation to major glaciations (blue) and continental breakup events (beige). Red bars signify major volcanic events involving extensive hyaloclastite emplacement (see Supplementary Table 1 for more information); note LIP, Large Igneous Province; ANS, Arabian-Nubian Shield.

subaqueous hyaloclastites, breccias and lavas emplaced along the rifted northwestern Laurentian margin³¹—is directly overlain by Sturtian glacial diamictites. Rift-related volcanism would have continued during glaciations (Supplementary Table 1), as newly formed ocean crust progressively unzipped to form the extensive Proto-Pacific ridge system. Crucially, and in contrast to most other biogeochemical fluxes, hyaloclastite-derived ocean fluxes will not have been affected by near-global ice cover.

There is also evidence for extensive volcanism, again associated with Rodinia breakup, before the Marinoan glaciation (for example, 670–650 Ma in Antarctica⁷; Fig. 2). The apparent ‘delay’ in initiation of rifting between Laurentia and Antarctica confirms that breakup was protracted³, and seafloor spreading continued throughout the Sturtian and Marinoan glaciations. Similarly, basaltic hyaloclastites associated with the early opening of Iapetus (~615–580 Ma) are recognized globally (Fig. 2; Supplementary Table 1). Hyaloclastites are directly overlain by diamictites associated with the Gaskiers glaciation³², signifying explosive shallow marine volcanism before (and probably during) the Gaskiers event (Fig. 2).

Better time constraints in the Neoproterozoic are needed to explore whether shallow-ridge volcanism could have played a key role in initiating snowball glaciation. However, this is feasible given an intrinsic need for continental breakup to intensify silicate weathering^{4,10}, and isotopic evidence for copious weathering of juvenile mantle-derived volcanics before the Sturtian glaciation³³.

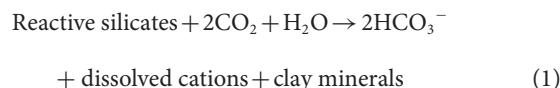
Hyaloclastite alteration fluxes into the ocean

We develop Monte Carlo simulations to quantify potential chemical fluxes (Ca, P, Si, Mg) into the ocean during shallow-ridge

volcanism. Given the significant uncertainties in initial conditions and fluxes (for example, sea-water chemistry, pH), this situation does not lend itself to deterministic modelling, but instead must be probabilistically assessed. Here, we present a parsimonious model, supported by observations and experiments (Table 1, Methods), broadly capturing the key processes and associated uncertainties. Ridge length is varied from $0.5\text{--}2 \times 10^4$ km to simulate progressive separation of Laurentia³, and full spreading rates from $50\text{--}200$ mm yr⁻¹ to represent moderate³⁴ to fast³⁵ rates expected during breakup⁵. The simulations account for secondary mineral formation, for example, carbonate fluorapatite (CFA) formation following release of P₂O₅ during glass alteration, and smectite (saponite) formation as a sink for silica. Fluxes calculated here exclude background seafloor weathering and hydrothermal processes³⁶ associated with contemporary deep-ridge systems, for example, in the Mirovia superocean (Fig. 1a), which would increase Ca, P, Si and Mg oceanic input.

Hyaloclastite formation rates (and hence magnitude of the chemical fluxes) vary spatially and temporally during ridge formation, hence our deliberately wide and conservative parameter ranges (Table 1). All input distributions are sampled independently because of insufficient observational evidence to accurately define correlations, but three more tightly constrained scenarios (Supplementary Table 2) explore sensitivity of the calculated fluxes to independence assumptions. The high-hyaloclastite-production scenario (Supplementary Table 2) involves both rapid and spatially extensive unzipping. A further simulation explores the potential correlation between ridge length and magmatic productivity, arising from the temporal evolution of the ridge system.

Given CaO losses from hyaloclastites range from 4–10 wt% (refs 24,25), our simulations suggest optimal spreading conditions along the length of the Proto-Pacific ridge could yield a maximum Ca flux of 1.4×10^{13} mol yr⁻¹ (Fig. 3a; Supplementary Fig. 3a); comparable to the modern dissolved riverine flux of $\sim 1.2 \times 10^{13}$ mol yr⁻¹ (ref. 37) and one to three orders of magnitude greater than the modern hydrothermal ridge flux ($9\text{--}1,300 \times 10^9$ mol yr⁻¹; ref. 38). Glass alteration also results in uptake of CO₂ from solution³⁹ according to the approximate reaction:



Ca forms most of the charge balance carried by the dissolved cation budget released to solution during glass alteration. Mg and Na contribute most of the remainder, along with a small uptake of K (ref. 24). Thus, a combined Ca, Mg and Na (–K) flux of approximately 2×10^{13} mol yr⁻¹ during hyaloclastite alteration results in uptake of 4×10^{13} mol yr⁻¹ of CO₂. By comparison, the global rate of continental silicate weathering is 1.2×10^{13} mol yr⁻¹ of CO₂ (ref. 40).

Hyaloclastite alteration in an ice-covered ocean provides a major source of alkalinity—additional to that provided by the long-term alteration of the oceanic crust²⁰—driving up carbonate production immediately after Snowball Earth glaciations. The cap carbonate sequences that formed globally on continental margins, typically overlying glacial diamictites^{2,12}, are commonly attributed to enhanced terrestrial weathering of carbonate-rich sediments during and after glaciation^{14,15}. However, to achieve observed cap carbonate thicknesses (some >100 m, Fig. 3c,d) would require extreme levels of terrestrial weathering, delivering $\sim 10^2\text{--}10^3$ times the present annual supply of dissolved cations to the oceans²⁹. Continental runoff during the post-snowball greenhouse ($400\times$ modern p_{CO_2}) probably produced ~ 1.2 times the modern riverine runoff¹⁶, suggesting subaerial weathering alone cannot explain cap carbonate production²⁹.

Table 1 | Ranges of parameter values used in the Monte Carlo simulations.

Sampled parameters	Minimum value	Maximum value
R = Ridge length (m) (ref. 3)	0.5×10^7	2×10^7
S = Spreading rate (m yr ⁻¹) (refs 5,34,35)	0.05	0.2
D = Alteration (penetration) depth (m) (ref. 36)	100	1,500
H_s = Fraction hyaloclastite from 0 to 1 km depth (ref. 23, Methods)	0.5	0.8
Φ_s = Hyaloclastite porosity (Φ) from 0 to 1 km depth (ref. 36)	0.12	0.3
H_d = Fraction hyaloclastite from 1 to 1.5 km depth (ref. 23, Methods)	0.1	0.2
Φ_d = Hyaloclastite porosity (Φ) from 1 to 1.5 km depth (ref. 36)	0.08	0.12
P = Altered (palagonite) fraction (refs 24,25)	0.6	1.0
L_{CaO} = Fraction CaO loss (refs 24,25)	0.04	0.1
L_{SiO_2} = Fraction SiO ₂ loss (refs 24,25)	0.1	0.3
$L_{P_2O_5}$ = Fraction P ₂ O ₅ loss (refs 24,25)	0.002	0.006
L_{MgO} = Fraction MgO loss (refs 24,25)	0.027	0.067
C_{CaO} , C_{CFA} , C_{SiO_2} , C_{MgO} = Cement phase (as fraction of element loss)	0	1.0

See Methods for further details.

We propose that under near-global ice cover, which suppresses normal removal processes, a prolonged state of hyaloclastite eruption and alteration would supersaturate sea water with Ca²⁺ and Mg²⁺. This is consistent with evidence for rapid carbonate sedimentation (spontaneous nucleation) following glaciations^{2,12,15}. The question is whether requisite degrees of supersaturation are feasible over such prolonged timescales (of the order of 10 Myr). At our maximum estimated discharge rate (the trivial case with no initial dissolved Ca²⁺ or Mg²⁺) the ocean reaches saturation within 1–3 Myr (Ca²⁺ and Mg²⁺, respectively). A 10 Myr glaciation could therefore yield degrees of supersaturation exceeding 12× (Ca²⁺) and 3× (Mg²⁺), certainly feasible in the light of observations of experimental solutions⁴¹, geologic fluids⁴², and the present-day surface ocean⁴³. In the glacial aftermath, conditions become more favourable for rapid precipitation: higher ocean temperatures, renewed photosynthesis, increased primary productivity, enhanced atmospheric CO₂ exchange and, importantly, resumption of particle settling providing carbonate condensation nuclei. Volcanism before and after glaciations (Fig. 2; Supplementary Table 1) will also have contributed to carbonate deposition, although in the absence of ice cover (limiting build-up in the ocean) would occur more gradually. Combined with the rate-limiting influence of platform subsidence², this may explain slower sedimentation rates inferred for some Marinoan carbonate sequences^{17,18}.

In an ice-covered ocean, limited atmospheric exchange leads to rapid conversion of dissolved CO₂ to bicarbonate (HCO₃⁻, which constitutes the majority of sea-water DIC) by equation (1). However, hyaloclastite formation is also associated with CO₂ degassing from erupted basalt, particularly at shallow depths. Assuming a pre-eruptive CO₂ concentration of 0.5 wt% in the basalts and total

degassing, hyaloclastite emplacement could release $\sim 0.03\text{--}1.3 \times 10^{12}$ mol yr⁻¹ CO₂, broadly consistent with the ridge flux ($\sim 0.8 \times 10^{12}$ mol yr⁻¹) assumed for the ‘snowball’ ocean². This is not a completely closed system: cracks in sea ice⁴⁴ will have permitted some CO₂ outgassing. Equally, ice-free regions will have allowed CO₂ ingassing during a period when atmospheric CO₂ levels due to subaerial volcanism² ultimately exceeded present-day levels by two to three orders of magnitude¹¹, a net CO₂ gain. The long-term CO₂ input from volcanism and hydrothermal activity can explain mantle-like $\delta^{13}\text{C}$ signatures ($-6 \pm 1\%$) observed in many cap carbonates^{2,12,13}. Stratigraphic or localized carbonate $\delta^{13}\text{C}$ increases²⁹ may reflect increases in biological productivity, organic carbon burial, and intensified subaerial carbonate weathering—also expected in the snowball aftermath^{15,19}.

Some post-Sturtian cap carbonates exhibit ¹⁸⁷Os/¹⁸⁸Os ratios consistent with continental inputs³³, again expected during a post-glacial weathering spike. However, many cap carbonates exhibit only minor shifts in ⁸⁷Sr/⁸⁶Sr (refs 15,29), suggesting that enhanced terrestrial weathering was not dominant in their production²⁹. Pre-Marinoan carbonates (800–650 Ma) exhibit relatively low ⁸⁷Sr/⁸⁶Sr (ref. 45), compatible with significant hydrothermal ridge contributions⁴⁶, which will progressively dominate the Sr isotope inventory in sea water under ice cover with much reduced continental runoff¹⁵. Further, widespread enrichment of heavy rare earth elements (REE) and positive Eu and Y anomalies in Sturtian⁴⁷ and Marinoan⁴⁸ cap carbonates can be explained by alteration of mid-ocean ridge basalts and wholesale mixing of hydrothermal fluids in the ocean^{48,49}.

The maximum simulated Ca²⁺ flux (Fig. 3a) would yield ~ 18.5 -m-thick build-up (mean estimate 2 m, median 1.2 m, Fig. 3c) of carbonate over an area equivalent to the present-day continental shelf for every 10⁶ years of ridge formation. Given the Sturtian (diachronous⁵⁰) and Marinoan glaciations persisted for ~ 55 Myr (ref. 33) and ~ 12 Myr (ref. 51), respectively, these accumulations are of the same order as observed cap carbonates, typically metres to tens of metres thick¹² (Fig. 3c).

Ridge alteration could produce magnesium fluxes of the order of $1\text{--}6 \times 10^{12}$ mol yr⁻¹ (Fig. 3b and Supplementary Table 2; modern riverine Mg flux is 5.1×10^{12} mol yr⁻¹; ref. 37), potentially contributing $\sim 2\text{--}15$ -m-thick dolostone for every 10⁶ years of ridge formation. Accordingly, our model suggests the Marinoan event could yield 20–150-m-thick dolostone, consistent with observed global mean and maximum thicknesses of 18.5 m and 175 m respectively⁵² (Fig. 3d). On timescales typically associated with deglaciation (circa 10 kyr), continental weathering is likely to supply enough Mg²⁺ to produce only a ~ 0.5 -m-thick cap dolostone¹⁶. Therefore, our hypothesis provides an important or even dominant additional source of Ca²⁺ and Mg²⁺, and can help explain not only the qualitative association of cap carbonate and dolostone sequences with Snowball Earth episodes, but also observed thicknesses of these deposits.

Although up to 90% P₂O₅ in fresh basaltic glass can be released during alteration²⁵, we assume a conservative 20–80% loss, based on modern palagonites²⁴. Simulations show that high spreading rates (>100 mm yr⁻¹), coupled with extensive ridges ($>15 \times 10^3$ km), could yield dissolved phosphorus fluxes up to 7×10^{11} mol yr⁻¹ (Fig. 4a; Supplementary Fig. 3b), roughly 20 times the modern dissolved riverine flux (3.1×10^{10} mol yr⁻¹; ref. 37). For the full simulation (Supplementary Table 2), the median phosphorus flux (3.7×10^{10} mol yr⁻¹) is comparable to the modern riverine contribution, and the high-hyaloclastite-production scenario yields a flux ~ 7 times greater (2.3×10^{11} mol yr⁻¹; Fig. 4b). Assuming full unzipping and substantial secondary mineralization losses (Supplementary Fig. 4), there is $\sim 70\%$ probability that P-influx would exceed the modern riverine flux (Supplementary Fig. 5). In the modern ocean, phosphate sorption onto ferric oxyhydroxides

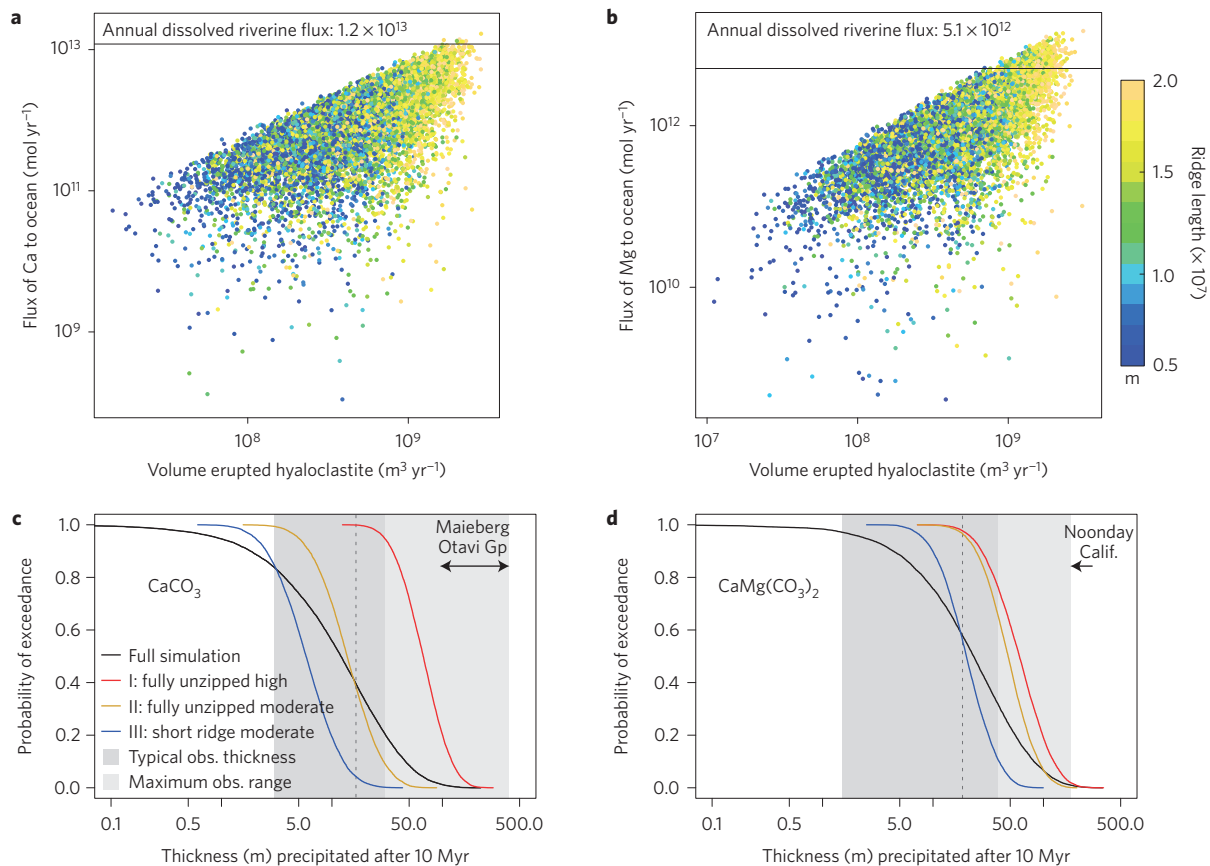


Figure 3 | Monte Carlo simulations showing estimated Ca and Mg fluxes into the 'snowball' ocean, and resulting thicknesses of carbonate and dolostone. Input parameter ranges are defined in Table 1. Note the logarithmic scales for the flux axes in **a,b**. **a**, Flux of Ca, accounting for a variable percentage lost to CaCO_3 cementation. **b**, Flux of Mg, accounting for in situ dolomite cementation; lines denote the modern annual riverine dissolved Ca and Mg fluxes for comparison. Note that **a** and **b** represent the full simulation (Supplementary Table 2). **c,d**, Probability of exceedance for cap carbonate (**c**) and dolostone (**d**) thicknesses resulting from accumulation of Ca and Mg, respectively, in sea water over the course of a Snowball Earth episode of 10 Myr duration. The shaded areas show typical (grey) and maximum (light grey) observed thicknesses: 3–30 m for CaCO_3 (maximum 400 m; ref. 12) and 1.5–38 m for $\text{CaMg}(\text{CO}_3)_2$ (maximum >175 m; ref. 52). The curves show the probability, based on all simulations, that a given thickness will be exceeded; for example, for the full simulation (black line) shown in **c**, more than 40% of simulations exceed the observed mean of carbonate thickness (~18.5 m; shown as a dashed line), and 20% exceed 30 m. Curves are shown for the full simulation (black line) and three alternative ridge productivity scenarios (I–III) defined in Supplementary Table 2.

represents a significant sink, but this is thought to have been of minor importance in the Neoproterozoic owing to high oceanic silicic acid concentrations—as silica hydroxides suppress phosphate sorption onto ferric oxyhydroxides¹⁹.

Hyaloclastite alteration during ridge unzipping provides a viable mechanism to account for anomalously high sea-water phosphorus levels (five to ten times Phanerozoic levels, according to P:Fe ratios in sedimentary iron formations; ref. 19) inferred for Snowball Earth episodes. This 'excess phosphate ocean' has been attributed to enhanced weathering of glacial deposits during the 'snowball' thaw phase¹⁹. Although relevant, post-glacial weathering would be expected to yield a relatively short-lived (~10–100 kyr; ref. 16) increase in phosphate, and could be problematic in view of the low solubility of apatite. Our model provides a mechanism for producing high dissolved phosphorus levels that, in the absence of biological removal, could persist over ~10–100 Myr (Fig. 2), over repeated cycles (that is, protracted opening of the Proto-Pacific followed by Iapetus in Ediacaran times; Fig. 1b; ref. 3). This process operated independently, and in addition to other mechanisms, such as biotic enhancement of apatite weathering linked to increased weathering rates via microbial colonization of the land⁵³, and subaerial weathering of large igneous provinces⁵⁴ (notably during the Tonian period; Fig. 2).

The shallow ridge can also contribute to relatively high dissolved oceanic silicic acid concentrations inferred for the Neoproterozoic¹⁹, and the SiO_2 -rich (~30–55%) BIFs that served as a (local) silica sink during the Sturtian^{30,55}, and possibly, but not ostensibly, during the Marinoan⁵⁵ glaciations. Basaltic glass alteration results in loss of an average ~16 wt% SiO_2 (ref. 24) (potentially up to 50%; ref. 25), thus contributing up to ten times the current riverine flux of $\sim 6.4 \times 10^{12}$ mol yr^{-1} (ref. 37) to the ocean during extensive hyaloclastite alteration (Supplementary Table 2, Supplementary Fig. 6b). High hydrothermal Fe fluxes⁴⁸ are expected in our low-hydrostatic-pressure regime⁵⁶, and a dominance of hydrothermal inputs is supported by mantle-like Nd and Pb isotope signatures observed in some BIFs (ref. 30). Thus, our hypothesis might help elucidate the common association between BIFs and mafic volcanics⁵⁵, although this requires further validation, particularly given the localized nature of many BIFs.

Consequences of a shallow-ridge system

The discovery that Earth experienced near-total ice cover for prolonged periods in the Neoproterozoic has greatly enhanced understanding of Earth history, but critical aspects remain unresolved. We demonstrate how enhanced shallow marine volcanic activity, persisting for >20 Myr in the absence of most

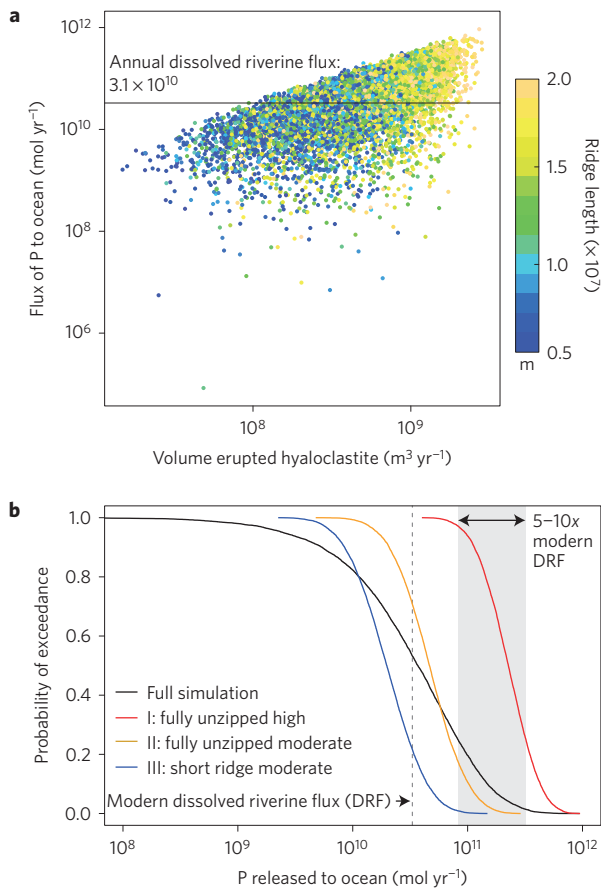


Figure 4 | Monte Carlo simulations for estimated phosphorus fluxes into a typical 'snowball' ocean. Input parameter ranges are defined in Table 1. Note the logarithmic scale for the flux axis in **a**. **a**, Flux of P, accounting for CFA cementation (Supplementary Fig. 4). Solid line denotes the modern annual dissolved riverine P flux for comparison³⁷. **b**, Probability of exceedance of phosphorus fluxes computed for the full simulation (black line) and three alternative ridge productivity scenarios (I–III) defined in Supplementary Table 2 (see Supplementary Fig. 5 for the effects of CFA cementation).

biological removal processes, would have driven major changes in ocean chemistry. Our shallow-ridge hypothesis advances understanding of Snowball Earth events, qualitatively and quantitatively explaining many enigmatic features including: increased ocean alkalinity; ¹³C-depleted cap carbonate sequences; and high silica concentrations manifest in banded iron formations.

Our hypothesis provides a critical quantitative explanation for unusually high dissolved phosphate inputs to late Proterozoic oceans. This enhanced supply may have driven the increase in primary productivity required to generate the large rise in atmospheric oxygen levels that occurred in the wake of Snowball Earth events¹⁹. We infer that shallow-ridge volcanism associated with the Proto-Pacific and Iapetan rifts also prompted oxidation of the Ediacaran ocean⁵⁷, which would have facilitated the emergence of multicellular life.

Methods

Methods and any associated references are available in the [online version of the paper](#).

Received 7 August 2015; accepted 10 December 2015;
published online 18 January 2016

References

- Kirschvink, J. L. in *The Proterozoic Biosphere: A Multidisciplinary Study* (eds Schopf, J. W. & Klein, C.) 51–52 (Cambridge Univ. Press, 1992).
- Hoffman, P. F., Kaufman, A. J., Halverson, G. P. & Schrag, D. P. A Neoproterozoic Snowball Earth. *Science* **281**, 1342–1346 (1998).
- Eyles, N. & Januszczak, N. 'Zipper-rift': a tectonic model for Neoproterozoic glaciations during the breakup of Rodinia after 750 Ma. *Earth Sci. Rev.* **65**, 1–73 (2004).
- Donnadieu, Y., Godderis, Y., Ramstein, G., Nedelec, A. & Meert, J. A 'Snowball Earth' climate triggered by continental break-up through changes in runoff. *Nature* **428**, 303–306 (2004).
- Torsvik, T. H. *et al.* Continental break-up and collision in the Neoproterozoic and Palaeozoic—a tale of Baltica and Laurentia. *Earth Sci. Rev.* **40**, 229–258 (1996).
- Macdonald, F. A. *et al.* Calibrating the Cryogenian. *Science* **327**, 1241–1243 (2010).
- Cooper, A. F., Maas, R., Scott, J. M. & Barber, A. J. W. Dating of volcanism and sedimentation in the Skelton Group, Transantarctic Mountains: implications for the Rodinia–Gondwana transition in southern Victoria Land, Antarctica. *Geol. Soc. Am. Bull.* **123**, 681–702 (2011).
- O'Brien, T. M. & van der Pluijm, B. A. Timing of Iapetus Ocean rifting from Ar geochronology of pseudotachylytes in the St. Lawrence rift system of southern Quebec. *Geology* **40**, 443–446 (2012).
- Van Staal, C. R., Dewey, J. F., MacNiocaill, C. & McKerrow, W. S. The Cambrian–Silurian tectonic evolution of the northern Appalachians and British Caledonides: history of a complex, west and southwest Pacific-type segment of Iapetus. *Geol. Soc. Lond. Spec. Publ.* **143**, 197–242 (1998).
- Goddéris, Y. *et al.* The Sturtian 'snowball' glaciation: fire and ice. *Earth Planet. Sci. Lett.* **211**, 1–12 (2003).
- Pierrehumbert, R. T. High levels of atmospheric carbon dioxide necessary for the termination of global glaciation. *Nature* **429**, 646–649 (2004).
- Hoffman, P. F. & Schrag, D. P. The Snowball Earth hypothesis: testing the limits of global change. *Terra Nova* **14**, 129–155 (2002).
- Halverson, G. P. & Shields-Zhou, G. Chapter 4 Chemostratigraphy and the Neoproterozoic glaciations. *Geol. Soc. Lond. Mem.* **36**, 51–66 (2011).
- Fairchild, I. J. Balmly shores and icy wastes: the paradox of carbonates associated with glacial deposits in Neoproterozoic times. *Sedimentol. Rev.* **1**, 1–16 (1993).
- Higgins, J. A. & Schrag, D. P. Aftermath of a Snowball Earth. *Geochem. Geophys. Geosyst.* **4**, 1028 (2003).
- Le Hir, G. *et al.* The Snowball Earth aftermath: exploring the limits of continental weathering processes. *Earth Planet. Sci. Lett.* **277**, 453–463 (2009).
- Trindade, R. I. F., Font, E., D'Agrella-Filho, M. S., Nogueira, A. C. R. & Riccomini, C. Low-latitude and multiple geomagnetic reversals in the Neoproterozoic Puga cap carbonate, Amazon craton. *Terra Nova* **15**, 441–446 (2003).
- Kennedy, M. J. & Christie-Blick, N. Condensation origin for Neoproterozoic cap carbonates during deglaciation. *Geology* **39**, 319–322 (2011).
- Planavsky, N. J. *et al.* The evolution of the marine phosphate reservoir. *Nature* **467**, 1088–1090 (2010).
- Le Hir, G., Ramstein, G., Donnadieu, Y. & Goddéris, Y. Scenario for the evolution of atmospheric p_{CO_2} during a Snowball Earth. *Geology* **36**, 47–50 (2008).
- Storey, M., Duncan, R. A. & Tegner, C. Timing and duration of volcanism in the North Atlantic Igneous Province: implications for geodynamics and links to the Iceland hotspot. *Chem. Geol.* **241**, 264–281 (2007).
- Planke, S., Symonds, P. A., Alvestad, E. & Skogseid, J. Seismic volcanostratigraphy of large-volume basaltic extrusive complexes on rifted margins. *J. Geophys. Res.* **105**, 19335–19351 (2000).
- Batiza, R. & White, J. D. L. in *Encyclopedia of Volcanoes* (ed. Sigurdsson, H.) 361–381 (Academic, 2000).
- Stronck, N. A. & Schmincke, H. U. Palagonite—a review. *Int. J. Earth Sci.* **91**, 680–697 (2002).
- Staudigel, H. & Hart, S. R. Alteration of basaltic glass: mechanisms and significance for the oceanic crust–sea water budget. *Geochim. Cosmochim. Acta* **47**, 337–350 (1983).
- Brady, P. V. & Gíslason, S. R. Seafloor weathering controls on atmospheric CO_2 and global climate. *Geochim. Cosmochim. Acta* **61**, 965–973 (1997).
- Mottl, M. J. & Wheat, C. G. Hydrothermal circulation through mid-ocean ridge flanks: fluxes of heat and magnesium. *Geochim. Cosmochim. Acta* **58**, 2225–2237 (1994).
- Jakobsson, S. P. Environmental factors controlling the palagonitization of the tephra of the Surtsey volcanic island, Iceland. *Bull. Geol. Soc. Denmark* **27**, 91–105 (1978).
- Kennedy, M. J., Christie-Blick, N. & Prave, A. R. Carbon isotopic composition of Neoproterozoic glacial carbonates as a test of paleoceanographic models for Snowball Earth phenomena. *Geology* **29**, 1135–1138 (2001).

30. Stern, R. J., Mukherjee, S. K., Miller, N. R., Ali, K. & Johnson, P. R. ~750 Ma banded iron formation from the Arabian–Nubian Shield—Implications for understanding Neoproterozoic tectonics, volcanism, and climate change. *Precambrian Res.* **239**, 79–94 (2013).
31. Cox, G. M. *et al.* in *Yukon Exploration and Geology 2012* (eds MacFarlane, K. E., Nordling, M. G. & Sack, P. J.) 19–36 (Yukon Geological Survey, 2013).
32. Calver, C. R., Black, L. P., Everard, J. L. & Seymour, D. B. U–Pb zircon age constraints on late Neoproterozoic glaciation in Tasmania. *Geology* **32**, 893–896 (2004).
33. Rooney, A. D. *et al.* Re–Os geochronology and coupled Os–Sr isotope constraints on the Sturtian Snowball Earth. *Proc. Natl Acad. Sci. USA* **111**, 51–56 (2014).
34. Reid, I. & Jackson, H. R. Oceanic spreading rate and crustal thickness. *Mar. Geophys. Res.* **5**, 165–172 (1981).
35. Wilson, D. S. Fastest known spreading on the Miocene Cocos–Pacific Plate boundary. *Geophys. Res. Lett.* **23**, 3003–3006 (1996).
36. Alt, J. C. in *Seafloor Hydrothermal Systems: Physical, Chemical, Biological, and Geological Interactions* number 91 (eds Humphris, S. E., Zierenberg, R. A., Mullineaux, L. S. & Thomson, R. E.) 85–114 (American Geophysical Union, 1995).
37. Berner, E. K. & Berner, R. A. *Global Environment: Water, Air, and Geochemical Cycles* 2nd edn (Princeton Univ. Press, 2012).
38. Elderfield, H. & Schultz, A. Mid-ocean ridge hydrothermal fluxes and the chemical composition of the ocean. *Annu. Rev. Earth Planet. Sci.* **24**, 191–224 (1996).
39. Wallmann, K. *et al.* Silicate weathering in anoxic marine sediments. *Geochim. Cosmochim. Acta* **72**, 2895–2918 (2008).
40. Gaillardet, J., Dupré, B., Louvat, P. & Allègre, C. J. Global silicate weathering and CO₂ consumption rates deduced from the chemistry of large rivers. *Chem. Geol.* **159**, 3–30 (1999).
41. Pokrovsky, O. Precipitation of calcium and magnesium carbonates from homogeneous supersaturated solutions. *J. Cryst. Growth* **186**, 233–239 (1998).
42. Compton, J. S. Degree of supersaturation and precipitation of organogenic dolomite. *Geology* **16**, 318–321 (1988).
43. Pokrovsky, O. S. Kinetics of CaCO₃ homogeneous precipitation in seawater. *Mineral. Mag.* **58A**, 738–739 (1994).
44. Allen, P. A. & Etienne, J. L. Sedimentary challenge to Snowball Earth. *Nature Geosci.* **1**, 817–825 (2008).
45. Kaufman, A. J., Jacobsen, S. B. & Knoll, A. H. The Vendian record of Sr and C isotopic variations in seawater: implications for tectonics and paleoclimate. *Earth Planet. Sci. Lett.* **120**, 409–430 (1993).
46. Halverson, G. P., Dudás, F. Ö., Maloof, A. C. & Bowring, S. A. Evolution of the ⁸⁷Sr/⁸⁶Sr composition of Neoproterozoic seawater. *Palaeogeogr. Palaeoclimatol. Palaeoecol.* **256**, 103–129 (2007).
47. Meyer, E. E., Quicksall, A. N., Landis, J. D., Link, P. K. & Bostick, B. C. Trace and rare earth elemental investigation of a Sturtian cap carbonate, Pocatello, Idaho: evidence for ocean redox conditions before and during carbonate deposition. *Precambrian Res.* **192–195**, 89–106 (2012).
48. Huang, J., Chu, X., Jiang, G., Feng, L. & Chang, H. Hydrothermal origin of elevated iron, manganese and redox-sensitive trace elements in the c. 635 Ma Doushantuo cap carbonate. *J. Geol. Soc.* **168**, 805–816 (2011).
49. Young, G. M. Precambrian supercontinents, glaciations, atmospheric oxygenation, metazoan evolution and an impact that may have changed the second half of Earth history. *Geosci. Front.* **4**, 247–261 (2013).
50. Kendall, B., Creaser, R. A. & Selby, D. Re–Os geochronology of postglacial black shales in Australia: constraints on the timing of ‘Sturtian’ glaciation. *Geology* **34**, 729–732 (2006).
51. Bodiselitsch, B., Koeberl, C., Master, S. & Reimold, W. U. Estimating duration and intensity of Neoproterozoic snowball glaciations from Ir anomalies. *Science* **308**, 239–242 (2005).
52. Hoffman, P. F. *et al.* Are basal Ediacaran (635 Ma) post-glacial ‘cap dolostones’ diachronous? *Earth Planet. Sci. Lett.* **258**, 114–131 (2007).
53. Lenton, T. M. & Watson, A. J. Biotic enhancement of weathering, atmospheric oxygen and carbon dioxide in the Neoproterozoic. *Geophys. Res. Lett.* **31**, L05202 (2004).
54. Horton, F. Did phosphorus derived from the weathering of large igneous provinces fertilize the Neoproterozoic ocean? *Geochem. Geophys. Geosyst.* **16**, 1723–1738 (2015).
55. Cox, G. M. *et al.* Neoproterozoic iron formation: an evaluation of its temporal, environmental and tectonic significance. *Chem. Geol.* **362**, 232–249 (2013).
56. Kump, L. R. & Seyfried, W. E. Jr Hydrothermal Fe fluxes during the Precambrian: effect of low oceanic sulfate concentrations and low hydrostatic pressure on the composition of black smokers. *Earth Planet. Sci. Lett.* **235**, 654–662 (2005).
57. Fike, D. A., Grotzinger, J. P., Pratt, L. M. & Summons, R. E. Oxidation of the Ediacaran Ocean. *Nature* **444**, 744–747 (2006).

Acknowledgements

E.J.R. acknowledges Australian Research Council Laureate Fellowship FL1201 00050. We are grateful to R. S. J. Sparks, R. N. Taylor, C. N. Trueman, T. Lenton, I. Fairchild and G. Shields-Zhou for helpful discussions and suggestions. Supplementary Fig. 1 was illustrated by G. Hincks.

Author contributions

T.M.G. conceived and managed the research. T.K.H. developed and performed simulations with inputs from T.M.G., T.T., M.R.P. and E.J.R. The manuscript was written by T.M.G., with important contributions from all co-authors.

Additional information

Supplementary information is available in the [online version of the paper](#). Reprints and permissions information is available online at www.nature.com/reprints. Correspondence and requests for materials should be addressed to T.M.G.

Competing financial interests

The authors declare no competing financial interests.

Methods

Deposition of chemically easily weathered hyaloclastites will cause a major influx of Ca, P, Si and Mg, among other elements, into the oceans. Monte Carlo simulations were performed to capture the variation in the main depositional and weathering processes. Input parameters were sampled independently from uniform distributions over fixed intervals, given in Table 1 (using the Scythe C++ Statistical Library⁵⁸). Uniform distributions were chosen, as these yield the most conservative estimate of uncertainty, and there is not enough observational evidence to justify a more tightly constrained distribution (for example, specifying a central weighting would require knowledge of the mean and variance of the distribution). The model generates a volume of hyaloclastite ($\text{m}^3 \text{yr}^{-1}$), given a sampled total ridge length (R), spreading rate (S) and cumulative deposit thickness (D). The annual elemental flux estimates (Fig. 3a,b) are based on annual ridge output (fresh material along the hot ridge axis). Any subsequent contributions from previously unaltered erupted products are conservatively excluded. Long-term accumulation in the ocean (over the period of active rifting; Fig. 3c,d) is estimated by summing the (variable) annual elemental contributions over a period of 10 Myr, again a conservative estimate of the time during which we would expect extensive hyaloclastite formation and alteration. We therefore account for short-term fluctuations in calculating cumulative oceanic inputs, and potential deposit (cap carbonate) thickness. The ridge length is varied from 5–20 $\times 10^3$ km to simulate progressive breakup of Rodinia around the perimeter of Laurentia⁵. The spreading rate is varied from 0.05–0.2 m yr^{-1} to simulate moderate³⁴ to fast³⁵ rates expected during breakup²¹. Here, the higher rate is not unreasonable, given that Laurentia is known to have moved at speeds of 0.2 m yr^{-1} during the Ediacaran⁵.

Conservatively, we consider a range of alteration penetration depths from 100–1,500 m (ref. 36). Through analogy with ophiolite sequences, hyaloclastite deposit thickness and other parameters will vary with depth. In the upper kilometre, the hyaloclastite (that is, pyroclastic) fraction (H_s) ranges from 50 to 80% of the total bed depth, reflecting the observed tendency for enhanced explosivity in shallow water conditions (<1 km; refs 23,59). Below 1 km, hyaloclastites are expected to be less extensive (10–20% of bed depth) owing to an overriding tendency for intrusive processes at depth in ocean crust³⁶. Again, conservatively, we assume no hyaloclastite below 1.5 km. These estimates are consistent with deposits observed along analogous rifted margins^{22,60–62}. The equations used in simulations are given below (for definitions, see Table 1 and Supplementary Tables 3 and 4).

Equation (2) gives the total thickness of hyaloclastite deposits, and (3) the corresponding mass of hyaloclastite formed per year along the length of the ridge. Equation (4) gives the approximate mass of P_2O_5 , CaO, SiO_2 or MgO lost due to hyaloclastite alteration. This can either be released to the ocean or consumed during cement formation.

$$t_s = DH_s \left. \vphantom{t_s} \right\} D \leq 1,000(\text{m}) \quad t_s = 1,000H_s \left. \vphantom{t_s} \right\} D > 1,000(\text{m}) \quad (2)$$

$$t_d = 0 \left. \vphantom{t_d} \right\} D \leq 1,000(\text{m}) \quad t_d = (D - 1,000)H_d \left. \vphantom{t_d} \right\} D > 1,000(\text{m})$$

$$m_{\text{total}} = RS\rho_{\text{crust}}(t_s(1 - \Phi_s) + t_d(1 - \Phi_d)) \quad (3)$$

$$m_{\text{P}_2\text{O}_5/\text{CaO}/\text{SiO}_2/\text{MgO}} = m_{\text{total}} PL_{\text{P}_2\text{O}_5/\text{CaO}/\text{SiO}_2/\text{MgO}} \quad (4)$$

Hyaloclastite volume will also be affected by porosity, which below 1 km depth (Φ_d) is taken to range from 0.08 to 0.12 (ref. 23), and above 1 km (Φ_s), where there is less compaction, from 0.12 to 0.3 (refs 36,63). Given that the volcanic environment and regime will largely generate fine-grained glass particles, and considering the relatively high porosities and reactive surface areas, we consider an altered fraction (P) ranging from 0.6–1.0, again typical of natural examples⁶⁴. The resulting deposit is then subject to elemental losses (that is, flux into the ocean and cement formation). For example, Ca losses (L_{CaO}) are assumed to range from 0.04 to 0.1 of the altered fraction, as observed in natural samples^{24,64}. These input distributions represent the main processes affecting annual variability in elemental flux.

A component of the elemental losses will form pore-filling cements and the remainder is assumed to go directly into the ocean. Cement fraction (C_{CaO}) is highly variable in nature⁶⁵. We therefore allow it to range from 0 to 1.0 of the total amount of the leachate, and consider secondary phases that result in relatively high losses of elements. For calcium, we consider CaCO_3 containing ~56% CaO, whereas saponite clays (smectite) contain only ~1.2% CaO. This approach leads to a conservative estimate of ocean flux, particularly as cement formation typically takes place over longer timescales (>10⁵ yr; refs 64,65).

The model considers the formation of: carbonate fluorapatite (CFA) cement, with equation (5) giving the mass of P_2O_5 in cements, (6) the mass of CaO in cements, and (7) the total CFA cement mass; carbonate cement, with (8) giving the mass of CaO and (9) the total mass of CaCO_3 cement; saponite clays, with (10) giving the total mass of SiO_2 and (11) the total mass of saponite; and dolomite cement, with (12) giving the mass of MgO and (13) the total mass of $\text{CaMg}(\text{CO}_3)_2$ cement. In all cases the resulting mass released to the ocean is assumed to be $m^o = m - m^c$. The numbers of moles of Ca, P, Si and Mg released to the ocean are given in (14)–(17). Equation (18) gives the equivalent fraction of hyaloclastite pore space filled with cement or clay.

Carbonate fluorapatite (CFA) (kg yr^{-1}):

$$m_{\text{P}_2\text{O}_5}^c = C_{\text{CFA}} m_{\text{P}_2\text{O}_5} \quad (5)$$

$$m_{\text{CaO}}^c = \left(\frac{0.56}{0.36} \right) m_{\text{P}_2\text{O}_5}^c \quad (6)$$

$$m_{\text{CFA}}^c = \frac{100m_{\text{P}_2\text{O}_5}^c}{q_{\text{P}_2\text{O}_5}} \quad (7)$$

Carbonate cement (kg yr^{-1}):

$$m_{\text{CaO}}^c = C_{\text{CaO}} m_{\text{CaO}} \quad (8)$$

$$m_{\text{CaCO}_3}^c = m_{\text{CaO}}^c + \left(w_{\text{CO}_2}^{\text{mol}} \left(\frac{m_{\text{CaO}}^c}{w_{\text{CaO}}^{\text{mol}}} \right) \right) \quad (9)$$

Saponite-type clays (kg yr^{-1}):

$$m_{\text{SiO}_2}^c = C_{\text{SiO}_2} m_{\text{SiO}_2} \quad (10)$$

$$m_{\text{saponite}}^c = \frac{100m_{\text{SiO}_2}^c}{q_{\text{SiO}_2}} \quad (11)$$

Dolomite cements (kg yr^{-1}):

$$m_{\text{MgO}}^c = C_{\text{MgO}} m_{\text{MgO}} \quad (12)$$

$$m_{\text{CaMg}(\text{CO}_3)_2}^c = m_{\text{MgO}}^c + (2w_{\text{CO}_2}^{\text{mol}} + w_{\text{CaO}}^{\text{mol}}) \left(\frac{m_{\text{MgO}}^c}{w_{\text{MgO}}^{\text{mol}}} \right) \quad (13)$$

Flux to the ocean (mol yr^{-1}):

$$n_{\text{Ca}} = m_{\text{CaO}}^o \left(\frac{1,000}{w_{\text{CaO}}^{\text{mol}}} \right) \quad (14)$$

$$n_{\text{P}} = 2m_{\text{P}_2\text{O}_5}^o \left(\frac{1,000}{w_{\text{P}_2\text{O}_5}^{\text{mol}}} \right) \quad (15)$$

$$n_{\text{Si}} = m_{\text{SiO}_2}^o \left(\frac{1,000}{w_{\text{SiO}_2}^{\text{mol}}} \right) \quad (16)$$

$$n_{\text{Mg}} = m_{\text{MgO}}^o \left(\frac{1,000}{w_{\text{MgO}}^{\text{mol}}} \right) \quad (17)$$

Pore fill:

$$f_{\text{fill}} = \left(\frac{m^c / \rho_{\text{cement}}}{(\Phi_s v_s) + (\Phi_d v_d)} \right) \quad (18)$$

Input parameter distributions are deliberately and conservatively wide to simulate the full range of plausible conditions and high temporal and spatial variability during ridge formation. Ocean flux estimates for three variant scenarios are presented to demonstrate model sensitivity to basic assumptions: scenario I, corresponding to full unzipping with high hyaloclastite production, scenario II, corresponding to full unzipping with moderate hyaloclastite production and scenario III, corresponding to partial unzipping with moderate hyaloclastite production. Supplementary Table 2 presents the full range of input distributions for the full and variant scenarios.

Supplementary Fig. 3 shows the fluxes of calcium and phosphorus into the ocean as a function of spreading rate and accumulated deposit thickness (using full simulation values in Supplementary Table 2). Supplementary Fig. 4 shows estimated hyaloclastite volumes, and the effect of cementation on ocean flux of P. The specific effect of cementation on the phosphorus flux was also considered (Supplementary Fig. 5), and shows that even cases involving high degrees of cement formation can still result in very high dissolved phosphorus fluxes (relative to the modern riverine flux) for long ridges. Supplementary Fig. 6 shows probability of exceedance for Ca and Si for the variant scenarios (I, II and III in Supplementary Table 2), alongside the full simulation.

A further simulation explores sensitivity to the temporal evolution of the rifting process, accounting for probable (but difficult to constrain) correlations between ridge length and magmatic productivity. Here we define three phases in the rifting process, based on the parameters used for the full simulation (observed global, present-day averages): phase A, initiation, where ridge length is short ($R = 5,000$ – $10,000$ km) but productivity is high ($S = 0.15$ – 0.2 m yr^{-1} , $D = 1,000$ – $1,500$ m); phase B, mid-event ($R = 10,000$ – $15,000$ km, $S = 0.10$ – 0.15 m yr^{-1} , $D = 600$ – $1,000$ m); and phase C, final stages of rifting where the ridge has reached its full extent but productivity is very low ($R = 15,000$ – $20,000$ km, $S = 0.05$ – 0.10 m yr^{-1} , $D = 100$ – 600 m). All other

parameters are as defined in Supplementary Table 2 for the full simulation. Supplementary Fig. 7 shows the probability of exceedance for annual Ca flux for phases A, B and C, compared to the full simulation (shown in black). This shows that, although we cannot explicitly model correlations between parameters (for example, arising from temporal evolution), the full and variant scenarios provide a reasonable representation of cumulative fluxes over typical timescales associated with unzipping of Rodinia (of the order of 10 Myr). Unfortunately, there is insufficient observational evidence to apply covariance estimates to other parameters used in our simulations. In the absence of robust evidence, any attempt to correlate parameters (for example, cement fraction and depth) would decrease the uncertainty, thereby reducing the spread of the output distributions and providing false certainty in the outputs.

To reconcile the results of the simulation with observed post-snowball cap carbonate and dolostone deposits, we estimate the thickness of precipitates that could form after 10 Myr accumulation of oceanic Ca and Mg (Fig. 3c,d). Taking the simulated annual flux of Ca and Mg (mol yr^{-1}) as the average for the episode, and assuming a final depositional area equivalent to the modern day continental shelf ($A = 2.8 \times 10^{13} \text{ m}^2$) gives the following estimate for cumulative deposit thickness after 10 Myr:

$$T = n^{\text{mol}} \times 10^7 \left(\frac{w^{\text{mol}}}{1,000} \right) \left(\frac{1}{\rho A} \right) \quad (19)$$

where n^{mol} is the number of moles yr^{-1} from our simulation, w^{mol} is the molar weight of either carbonate, CaCO_3 (100 g mol^{-1}) or dolomite, $\text{CaMg}(\text{CO}_3)_2$ (184.4 g mol^{-1}), and ρ is the density of the deposit, that is, ρ_{CaCO_3} or ρ_{Dolo} (Supplementary Table 3).

Code availability. We have opted not to make the computer code associated with this paper available because it is being developed at present for another follow-up study, but will be released when this work is published.

References

58. Pemstein, D., Quinn, K. M. & Martin, A. D. The Scythe statistical library: an open source C++ library for statistical computation. *J. Stat. Softw.* **42**, 1–26 (2011).
59. Fisher, R. V. Submarine volcanoclastic rocks. *Geol. Soc. Lond. Spec. Publ.* **16**, 5–27 (1984).
60. Peate, I. U., Larsen, M. & Leshner, C. The transition from sedimentation to flood volcanism in the Kangerlussuaq Basin, East Greenland: basaltic pyroclastic volcanism during initial Palaeogene continental break-up. *J. Geol. Soc.* **160**, 759–772 (2003).
61. Bell, B. & Butcher, H. On the emplacement of sill complexes: evidence from the Faroe–Shetland Basin. *Geol. Soc. Lond. Spec. Publ.* **197**, 307–329 (2002).
62. Jerram, D. A., Single, R. T., Hobbs, R. W. & Nelson, C. E. Understanding the offshore flood basalt sequence using onshore volcanic facies analogues: an example from the Faroe–Shetland basin. *Geol. Mag.* **146**, 353–367 (2009).
63. Walton, A. W. & Schiffman, P. Alteration of hyaloclastites in the HSDP 2 Phase 1 Drill Core 1. Description and paragenesis. *Geochem. Geophys. Geosyst.* **4**, 8709 (2009).
64. Morton, A. C. & Keene, J. B. *DSDP Initial Reports* Vol. 81, Ch. 19, 633–643 (Ocean Drilling Program, 1984).
65. Desprairies, A., Bonnot-Courtois, C., Jehanno, C., Vernhet, S. & Joron, J. L. *DSDP Initial Reports* Vol. 81, Ch. 28, 733–742 (Ocean Drilling Program, 1984).